Manuscript
Click here to download Manuscript: G35892-Yang-formatted revised manuscript.doc

Publisher: GSA
Journal: GEOL: Geology
Article ID: G35892

Global continental weathering trends across the Early Permian glacial to post-glacial transition: Correlating high and low paleo-latitude sedimentary records

Jianghai Yang[1*], Peter A. Cawood[2,3], Yuansheng Du[1], Bin Feng[4], and Jiaxin Yan[1]

[1]State Key Laboratory of Biogeology and Environmental Geology, China University of Geosciences, Wuhan, 430074, China

[2]Department of Earth Sciences, University of St. Andrews, North Street, St. Andrews KY16 9AL, UK

[3]School of Earth and Environment, University of Western Australia, Crawley, WA 6009, Australia

[4]No.4 Institute of Geological & Mineral Resources Survey of Henan, Zhengzhou, 450016, China

ABSTRACT

Time equivalent Early Permian sedimentary successions from high latitude Gondwana basins and from equatorial accumulations in North China, covering the glacial to post-glacial transition, display correlatable trends in continental weathering intensity based on chemical index of alteration (CIA) values. The successions display a pattern of CIA values that varies with latitude similar to modern estuarine suspended sediments. Based on the modern day CIA-temperature correlation, the syn-glacial early Permian low to high latitude land surface temperature gradient is estimated at ~20 °C, slightly higher than the calculated values for the contemporaneous sea surface temperature gradient.

INTRODUCTION

Chemical weathering displays a strong dependence on climate and is favored in hot and humid conditions, but depressed in cold and dry climates (Nesbitt and Young, 1982). It converts primary labile silicate minerals to secondary clay and oxide-hydroxide minerals, resulting in modified whole-rock elemental abundances (e.g., Nesbitt and Markovics, 1997). The chemical index of alteration (CIA, Nesbitt and Young, 1982) is the most widely accepted index and is based on the proportion of secondary aluminous minerals relative to primary mineral phases. CIA provides an effective measure of weathering conditions at the source.

In this paper we present mineralogical, geochemical and geochronological data from a Lower Permian sedimentary sequence in North China, documenting continental weathering trends in these low-latitudinal sedimentary rocks and correlate them with contemporaneous high-latitude Gondwana records. Furthermore, we show that modern day differences in chemical weathering intensities between the low- and high-latitudinal sediments can be applied to the earliest Permian successions, yielding realistic estimates of the land surface temperature gradient. The Early Permian marks the end of the major high-latitude Gondwana glaciation and the transition to a post-glaciation climate state (Fielding et al., 2008; Isbell et al., 2012). This transition coincides with changes in sedimentology, fossil assemblages and sediment composition (Dickins, 1996; Wopfner, 1999), and with fluctuation in atmospheric CO_2 and O_2 contents (Glasspool and Scott, 2010; Montañez et al., 2007).

GEOLOGICAL SETTING AND SAMPLING SEQUENCE

The North China Craton occupied a near equatorial setting (~5–15 °) during the late Paleozoic (Fig. 1A; Huang et al., 2001). The craton formed through Paleoproterozoic suturing of Archean blocks and has constituted a stable platform since the Mesoproterozoic. Uplift in the early Paleozoic resulted in a major hiatus across the platform, and subsequent late Paleozoic transgression resulted in the deposition of widespread Late Carboniferous-Permian littoral, coal-bearing, clastic-dominated sequences (Wang, 1985). Drill core through the early Permian strata within the Yongcheng basin in southeastern North China yielded a continuous section that has escaped modern weathering. The sampled upper Shanxi Formation and conformably overlying Xiashihezi Formation consist of fine-grained sandstone, siltstone and black-pale gray mudstone with coal-seams up to several meters thick (Fig. 1b) that accumulated in a deltaic environment (Feng, 2012).

Methods

Whole-rock major and trace element concentrations were determined by XRF and ICP-MS, and mineralogical compositions were analyzed by XRD. Tuffaceous sandstone at the top Shanxi Formation was sampled for zircon LA-ICPMS dating. Analytical details and data are listed in the GSA Data Repository[1].

RESULTS

Dated zircons are elongate and euhedral with well-developed oscillatory zoning (Fig. DR1A). Th/U ratios are 0.55–1.63, indicating a volcanic origin (Table DR1). The youngest 21 analyses with concordance of 95% or greater yielded an age of 293.0 ± 2.5 Ma (MSWD = 0.57) (Fig. DR1B), and is interpreted as the crystallization age of the tuff. This age constrains the Shanxi Formation to the Asselian-Sakmarian on the timescale of Gradstein et al. (2012).

Silt-mudstone samples are mainly composed of clay minerals and quartz, with little or no feldspar (0-6%) and calcite (0-2%) (Table DR2). High siderite contents occur in three samples. Identified clay minerals include kaolinite, chlorite and illite. Kaolinite displays a negative relation with both chlorite and illite, and increases significantly from 50%–70% in the upper Shanxi Formation to 70%–80% in the lower Xiashihezi Formation (except for two samples with relatively high chlorite contents), and then decreases to 40%–70% for most samples in the upper Xiashihezi Formation (Fig. DR2).

Calculated CIA values using the silica-bound calcium correction (Nesbitt and Young, 1982, Fedo et al., 1995; McLennan, 1993) for silt-mudstone samples show a sharp increase from 87.8 to 91.3 for the upper Shanxi Formation to 91.8–98.0 for the lower Xiashihezi Formation and then a gradual decrease to 81.7–92.0 for the upper Xiashihezi Formation. This variation is consistent with those of other weathering indices (e.g., plagioclase index of alteration, Fedo et al., 1995) and kaolinite contents (Fig. DR2). Zr/Ti ratios, largely controlled by source rock composition (e.g., Scheffler et al., 2003), are relatively constant (Fig. DR2) and have no discernible co-variation with chemical weathering indices in the Lower Permian sequence. On the Al_2O_3-CaO+Na_2O-K_2O (A-CN-K) plot (Nesbitt and Young, 1984; Fedo et al., 1995) (Fig. 1C), the samples with CIA values of < 86 trend approximately parallel to the A-CN boundary, mimicking the predicted weathering trend (Nesbitt and Young, 1984). Samples with higher CIA values (CIA > ~86) lie subparallel to the A-K boundary but gradually tend toward the A apex. On the A-CN-K diagram the linear trend through the data points (sub)parallel to the A-CN boundary extends back to a point at which the proportion of plagioclase and K-feldspar are considered representative of the original parent rock composition (Fedo et al., 1995). This trend corresponds to the composition of the upper crust of southern North China (Gao et al., 1998) (Fig. 1C), the inferred source, and is consistent with facies reconstruction (Wang, 1985).

CORRELATIONS

In the Early Permian, Gondwana occupied mid- to high southern hemisphere paleo-latitudes (Fig. 1, Torsvik and Cocks, 2004). Periodic glaciations are recorded in the sedimentary successions of the Karoo (Scheffler et al., 2006), Kalahari (Scheffler et al., 2006), Ruhuhu (Diekmann and Wopfner, 1996), Paraná (Goldberg and Humayun, 2010), Satpura (Roy and Roser, 2013), Khalaspir basins (Ghosh and Sarkar, 2010) and Spiti Basin (Ganai et al., 2014) (Fig. 1). End Carboniferous-Permian Gondwana successions in these basins all exhibit a significant CIA increase at the Early Permian glacial to post-glacial transition (Fig. 2), corresponding to the demise of the earliest Permian ice sheets (Isbell et al., 2012), and signify enhancement of continental weathering. This climatic event is constrained biostratigraphically to the end Sakmarian-Artinskian and by ion microprobe zircon dating in the Karoo Basin to around 290 Ma (Bangert et al., 1999). The elevated CIA values diminish by the Kungurian, around ~281 Ma on the basis of a zircon U-Pb age from the Paraná Basin (Mori et al., 2012).

Our new zircon age from the Yongcheng Basin indicates that the boundary between the Shanxi and Xiashihezi formations correlates, within error, with the glacial to post-glacial transition in the Gondwana successions. This correlation indicates that the end-Sakmarian marks a significant rise in sediment CIA values in both low- and high-latitude locations and is a global signature (Fig. 2). The rise in CIA values also corresponds with an increase in atmospheric CO_2 content (Fig. 2; Montañez et al., 2007) and the global negative shift in seawater oxygen isotopes (Fig. 2; Korte et al., 2005; Korte et al., 2008). A subsequent decrease in CIA values is shown by both the North China and Gondwana sequences and has been related to intensifying aridity (Goldberg and Humayun, 2010) and/or a resumption of cold climate conditions (Fielding et al., 2008), and is accompanied by corresponding variation of atmospheric pCO_2 and seawater $\delta^{18}O$ (Fig. 2).

DISCUSSION

Extrapolation of chemical proxy data to degree of weathering is influenced by sedimentary and tectonic processes (e.g., Rieu et al., 2007; Scheffler et al., 2003). The potential effect of such variables on weathering index of samples from the North China craton is minimized by the stable tectonic setting, the uniform source composition with derivation from within the craton, the absence of any evidence for significant potassium metasomatism (Fig. 1C), and analyses limited to lutite samples from fresh core. Therefore, chemical weathering index signatures and linked clay mineral assemblage variation provide a valid record of changes in chemical weathering conditions of the source related to climate variation. Greatly enhanced continental weathering during the deposition of the basal Xiashihezi Formation corresponds with basin deepening and a major marine transgression (Feng, 2012), consistent with the intensification of weathering and a post-glacial climate. Temporal correlation of the continental weathering trends in North

China with similar trends in Gondwana indicates a global phenomenon recording the glacial to post-glacial transition (Fig. 2), despite possible local tectonic influences on sediments, which might be averaged out by large catchment areas for the sampled basins. This event corresponds to a warming interval associated with high atmospheric CO_2 concentrations (up to 2500 ppmv), which are distinctly higher than the earliest Permian values (~300 ppmv) of averaged present atmospheric CO_2 levels and followed by a short-lived drop in the Artinskian (Montañez et al., 2007). Increasing temperature is characteristic of a glacial to post-glacial transition (Korte et al., 2008; Rieu et al., 2007). Such a CO_2-forcing climate change could be responsible for the continental weathering enhancement as manifested by the compiled sediment geochemical data (Fig. 2).

Modern large river estuary suspended sediment analyses show CIA values changing with latitude and land surface temperature (Li and Yang, 2010). We hypothesize a similar latitude-associated silicate weathering distribution in the earliest Permian glaciation, which is an interval with atmospheric CO_2 levels broadly similar to the present day average (Montañez et al., 2007). CIA-latitude and CIA-temperature correlations for modern estuary systems are depicted in figure 3, and North China and Gondwana basin data are also plotted on this diagram based on their CIA values. The obtained latitude ranges overlap with those determined from Early Permian paleogeographic constraints (Fig. 1, Torsvik and Cocks, 2004). Given this relationship, we estimate a low- to high-latitude land surface temperature (LST) gradient of ~20 °C and mid- to high-latitude LST gradient of ~10 °C for the earliest Permian glacial stage. The low- to high-latitude LST gradient is largely comparable with the result based on present day CO_2 concentration modeled by Gibbs et al. (2002) for the Sakmarian, but higher than the contemporaneous low- to high-latitude sea surface temperature gradient of ~9–12 °C given by Korte et al. (2008), likely reflecting differences in the heat transport efficiency between the oceans and the atmosphere. The smaller difference in CIA values between the post-glacial low- and high-latitude basins (Fig. 2) likely denotes a subdued temperature gradient during that period.

CONCLUSIONS

A tuff zircon age and variations in CIA values from the Lower Permian sequence in North China enable correlation of this low-latitude sedimentary record with those in high-latitude Gondwana regions. Concomitant offset toward high CIA values in both high and low latitudinal successions reflects global climate change from a glacial to post-glacial state. Correlations of continental weathering with latitude and with temperature based on models from present day settings demonstrate a low- to high-latitude LST gradient of ~20 °C for the earliest Permian syn-glacial period.

ACKNOWLEDGMENTS

Editor Ellen Thomas and reviewers Grant M. Young, Karin Goldberg, Lorenz Schwark and Isabel P. Montañez are gratefully acknowledged for their constructive comments. We thank Zhaochu Hu for help with zircon LA-ICPMS dating and staff at the Yongcheng County core storage facility for help with sampling. This study was financially supported by National Science Foundation of China (Nos. 40921062 and 41302083), the ‘111project’ (No. B08030) and the Fundamental Research Funds for the Central Universities (CUGL140402).

REFERENCES CITED

Bangert, B., Stollhofen, H., Lorenz, V., and Armstrong, R., 1999, The geochronology and significance of ash-fall tuffs in the glaciogenic Carboniferous-Permian Dwyka Group of Namibia and South Africa: Journal of African Earth Sciences, v. 29, p. 33–49, doi:10.1016/S0899-5362(99)00078-0.

Dickins, J.M., 1996, Problems of a Late Paleozoic glaciation in Australia and subsequent climate in the Permian: Palaeogeography, Palaeoclimatology, Palaeoecology, v. 125, p. 185–197, doi:10.1016/S0031-0182(96)00030-2.

Diekmann, B., and Wopfner, H., 1996, Petrographic and diagenetic signatures of climatic change in peri- and postglacial Karoo Sediments of SW Tanzannia: Palaeogeography, Palaeoclimatology, Palaeoecology, v. 125, p. 5–25, doi:10.1016/0031-0182(95)00084-4.

Fedo, C.M., Nesbitt, H.W., and Young, G.M., 1995, Unraveling the effects of potassium metasomatism in sedimentary rocks and paleosols, with implications for paleoweathering conditions and provenance: Geology, v. 23, p. 921–924, doi:10.1130/0091-7613(1995)023<0921:UTEOPM>2.3.CO;2.

Feng, B., 2012, Study on coal-accumulating characteristic of Shanxi Formation and low Shihezi Formation in Yongcheng Coalfield: Henna Province: Journal of Henan Polytechnic University, v. 31, p. 177–181.

Fielding, C.R., Frank, T.D., Birgenheiner, L.P., Rygel, M.C., Jones, A.J., and Roberts, J., 2008, Stratigraphic imprint of the Late Paleozoic Ice Age in eastern Australia: A record of alternating glacial and nonglacial climate regime: Journal of the Geological Society, v. 165, p. 129–140, doi:10.1144/0016-76492007-036.

Ganai, J.A., Rashid, S.A., Alam, M.M., Balaram, V., and Sathyanarayanan, M., 2014, The geochemistry of Permo-Carboniferous black shales from Spiti region, Himachal Pradesh, Tethys Himalaya: A record of provenance and change in climate: Himalayan Geology, v. 35, no. 1, p. 31–39.

Gao, S., Luo, T., Zhang, B., Zhang, H., Han, Y., Zhao, Z., and Hu, Y., 1998, Chemical composition of the continental crust as revealed by studies in East China: Geochimica et Cosmochimica Acta, v. 62, p. 1959–1975, doi:10.1016/S0016-7037(98)00121-5.

Ghosh, S., and Sarkar, S., 2010, Geochemistry of Permo-Triassic mudstone of the Satpura Gondwana basin, central India: Clues for provenance: Chemical Geology, v. 277, p. 78–100, doi:10.1016/j.chemgeo.2010.07.012.

Gibbs, M.T., Rees, P.M., Kutzbach, J.E., Ziegler, A.M., Behling, P.J., and Rowley, D.B., 2002, Simulations of Permian climate and comparisioins with climate-sensitive sediments: The Journal of Geology, v. 110, p. 33–55, doi:10.1086/324204.

Goldberg, K., and Humayun, M., 2010, The applicability the Chemical Index of Alteration as a paleoclimatic indicator: An example from the Permian of the Paraná Basin, Brazil: Palaeogeography, Palaeoclimatology, Palaeoecology, v. 293, p. 175–183, doi:10.1016/j.palaeo.2010.05.015.

Glasspool, I.J., and Scott, A.C., 2010, Phanerozoic concentrations of atmospheric oxygen reconstructed from sedimentary charcoal: Nature Geoscience, v. 3, p. 627–630, doi:10.1038/ngeo923.

Gradstein, F.M., Ogg, J.G., Schmitz, M.D., and Ogg, G.M., 2012, The geological time scale 2012: Oxford, UK, Elsevier, p. 1144.

Huang, B., Otofuji, Y.I., Zhu, R., Shi, R., and Wang, Y., 2001, Paleomagnetism of Carboniferous sediments in the Hexi corridor: Its origin and tectonic implictions: Earth and Planetary Science Letters, v. 194, p. 135–149, doi:10.1016/S0012-821X(01)00557-X.

Isbell, J.L., Henry, L.C., Gulbranson, E.L., Limarino, C.O., Fraiser, M.L., Koch, Z.J., Ciccioli, P.L., and Dineen, A.A., 2012, Glacial paradoxes during the late Paleozoic ice age: evaluating the equilibrium line altitude as a control on glaciation: Gondwana Research, v. 22, p. 1–19, doi:10.1016/j.gr.2011.11.005.

Korte, C., Jasper, T., Kozur, H.W., and Veizer, J., 2005, $\delta^{18}O$ and $\delta^{13}C$ of Permian branchiopods: A record of seawater evolution and continenal glaciation: Palaeogeography, Palaeoclimatology, Palaeoecology, v. 224, p. 333–351, doi:10.1016/j.palaeo.2005.03.015.

Korte, C., Jones, P.J., Brand, U., Mertmann, D., and Veizer, J., 2008, Oxygen isotope values from high-latitudes: Clues for Permian sea-surface temperature gradients and late Paleozoic deglaciation: Palaeogeography, Palaeoclimatology, Palaeoecology, v. 269, p. 1–16, doi:10.1016/j.palaeo.2008.06.012.

Li, C., and Yang, S., 2010, Is chemical index of alteration (CIA) a reliable proxy for chemical weathering in global drainage basins?: American Journal of Science, v. 310, p. 111–127, doi:10.2475/02.2010.03.

Mahjoor, A.S., Karimi, M., and Rastegarlari, A., 2009, Mineralogical and geochemical characteristics of clay deposits from South Abarkouh district of clay deposit (Central Iran) and their applications: Journal of Applied Science, v. 9, no. 4, p. 601–614, doi:10.3923/jas.2009.601.614.

McLennan, S.M., 1993, Weathering and global denudation: The Journal of Geology, v. 101, p. 295–303, doi:10.1086/648222.

Montañez, I.P., Tabor, N.J., Niemeier, D., DiMichele, W.A., Frank, T.D., Fielding, C.R., Isbell, J.L., Birgenheier, L.P., and Rygel, M.C., 2007, CO_2-forced climate and vegetation instability during Late Paleozoic deglaciation: Science, v. 315, p. 87–91, doi:10.1126/science.1134207.

Mori, A.L.O., de-Souza, P.A., Marques, J.C., and Lopes, R.C., 2012, A new U-Pb zircon age dating and palynological data from a Lower Permian section of the southermost Paraná Basin, Brazil: biochronostratigraphical and geochronological implications for Gondwanan correlations: Gondwana Research, v. 21, p. 654–669, doi:10.1016/j.gr.2011.05.019.

Nesbitt, H.W., and Markovics, G., 1997, Weathering of granodioritic crust, long-term storage of elements in weathering profiles, and petrogenesis of siliciclastic sediments: Geochimica et Cosmochimica Acta, v. 61, p. 1653–1670, doi:10.1016/S0016-7037(97)00031-8.

Nesbitt, H.W., and Young, G.M., 1982, Early Proterozoic climates and plate motions inferred from major element chemistry of lutites: Nature, v. 299, p. 715–717, doi:10.1038/299715a0.

Nesbitt, H.W., and Young, G.M., 1984, Prediction of some weathering trends of plutonic and volcanic rocks based on thermodynamic and kinetic considerations: Geochimica et Cosmochimica Acta, v. 48, p. 1523–1534, doi:10.1016/0016-7037(84)90408-3.

Rieu, R., Allen, P.A., Plötze, M., and Pettke, T., 2007, Climatic cycles during a Neoproterozoic “snowball” glacial epoch: Geology, v. 35, p. 299–302, doi:10.1130/G23400A.1.

Roy, D.K., and Roser, B.P., 2013, Climatic control on the composition of Carboniferous-Permian Gondwana sediments, Khalaspir basin, Bangladesh: Gondwana Research, v. 23, p. 1163–1171, doi:10.1016/j.gr.2012.07.006.

Scheffler, K., Hoernes, S., and Schwark, L., 2003, Global changes during Carboniferous-Permian glaciation of Gondwana: linking polar and equatorial climate evolution by geochemical proxies: Geology, v. 31, p. 605–608, doi:10.1130/0091-7613(2003)031<0605:GCDCGO>2.0.CO;2.

Scheffler, K., Buehmann, D., and Schwark, L., 2006, Analysis of late Paleozoic glacial to postglacial sedimentary successions in South Africa by geochemical proxies—response to climate evolution and sedimentary environment: Palaeogeography, Palaeoclimatology, Palaeoecology, v. 240, p. 184–203, doi:10.1016/j.palaeo.2006.03.059.

Taylor, S.R., and McLennan, S.M., 1985, The continental crust: Its composition and evolution: Oxford, United Kingdom, Blackwell, 1–312 p.

Torsvik, T.H., and Cocks, L.R.M., 2004, Earth geography from 400 to 250 Ma: a paleomagnetic, faunal and facies review: Journal of the Geological Society, v. 161, p. 555–572, doi:10.1144/0016-764903-098.

Wang, H., 1985, Atlas of the palaeogeography of China: Beijing, Cartographic Publishing House, 74–80 p.

Wopfner, H., 1999, The Early Permian deglaciation event beween East Africa and northwestern Australia: Journal of African Earth Sciences, v. 29, p. 77–90, doi:10.1016/S0899-5362(99)00081-0.

FIGURE CAPTIONS

Figure 1. (A) Magneto- and fauna-based Early Permian paleogeographic map (Huang et al., 2001; Torsvik and Cocks, 2004) showing the approximate positions of the Yongcheng (black square) and the Gondwana basins (black stars: 1-Satpura Basin, 2-Khalaspir Basin, 3-Kalahari Basin, 4-Ruhuhu Basin, 5-Paraná Basin, 6-Karoo Basin, 7-Spiti Basin and 8-Central Iran Basin); (B) stratigraphic column of Core Zk1401 with analyzed samples, where filled circles, blank circles and filled star represent silt-mudstone, fine-grained sandstone and zircon dating sample sites, respectively; and (C) A-CN-K (Al_2O_3-CaO*+Na_2O-K_2O) diagram for the Lower Permian silt-mudstone (open circles) and fine-grained sandstone (open diamonds) samples, with CIA scale on the left side. Also plotted are the molar proportions of southern North China upper crust (SCN, Gao et al., 1998), interior North China upper crust (INC, Gao et al., 1998) and average upper continental crust (UCC, Taylor and McLennan, 1985).

Figure 2. Correlating CIA variation of the equatorial Early Permian pelitic sedimentary rocks from the Yongcheng Basin in North China with those from the mid-high latitude Khalaspir Basin (Roy and Roser, 2013), Satpura Basin (Ghosh and Sarkar, 2010), Karoo Basin (Scheffler et al., 2006), Kalahari Basin (Scheffler et al., 2006), Ruhuhu Basin (Diekmann and Wopfner, 1996), Paraná Basin (Goldberg and Humayun, 2010), Spiti Basin (Ganai et al., 2014) and Central Iran Basin (Mahjoor et al., 2009) in Gondwana. The zircon age data obtained by this study for the Yongcheng sequence, by Bangert et al. (1999) for the Karoo sequence, and by Mori et al. (2012) for the Paraná sequence, are marked according to their respective stratigraphic positions. Also shown are the temporal variations in inferred atmospheric CO_2 content (Montañez et al., 2007) and low- and high-latitudinal low-Mg calcite oxygen isotopic signature from fossil shells for comparison (Korte et al., 2005; Korte et al., 2008).

Figure 3. Plot of mean CIA values (green line) and deviations (gray box) for each of the studied and compiled earliest Permian sedimentary rocks with those from modern estuary suspended sediment CIA-latitude (A) and CIA-temperature (B) correlation models based on the compilation (black squares) of Li and Yang (2010). Abbreviations: YB-Yongcheng Basin, SB-Satpura Basin, SIB-Spiti Basin, PB-Paraná Basin, KB-Karoo Basin, KLB-Khalaspir Basin, and RB-Ruhuhu Basin.

[1]GSA Data Repository item 2014xxx, xxxxxxxx, is available online at www.geosociety.org/pubs/ft2014.htm, or on request from editing@geosociety.org or Documents Secretary, GSA, P.O. Box 9140, Boulder, CO 80301, USA.

Figure 1

Click here to download high resolution image

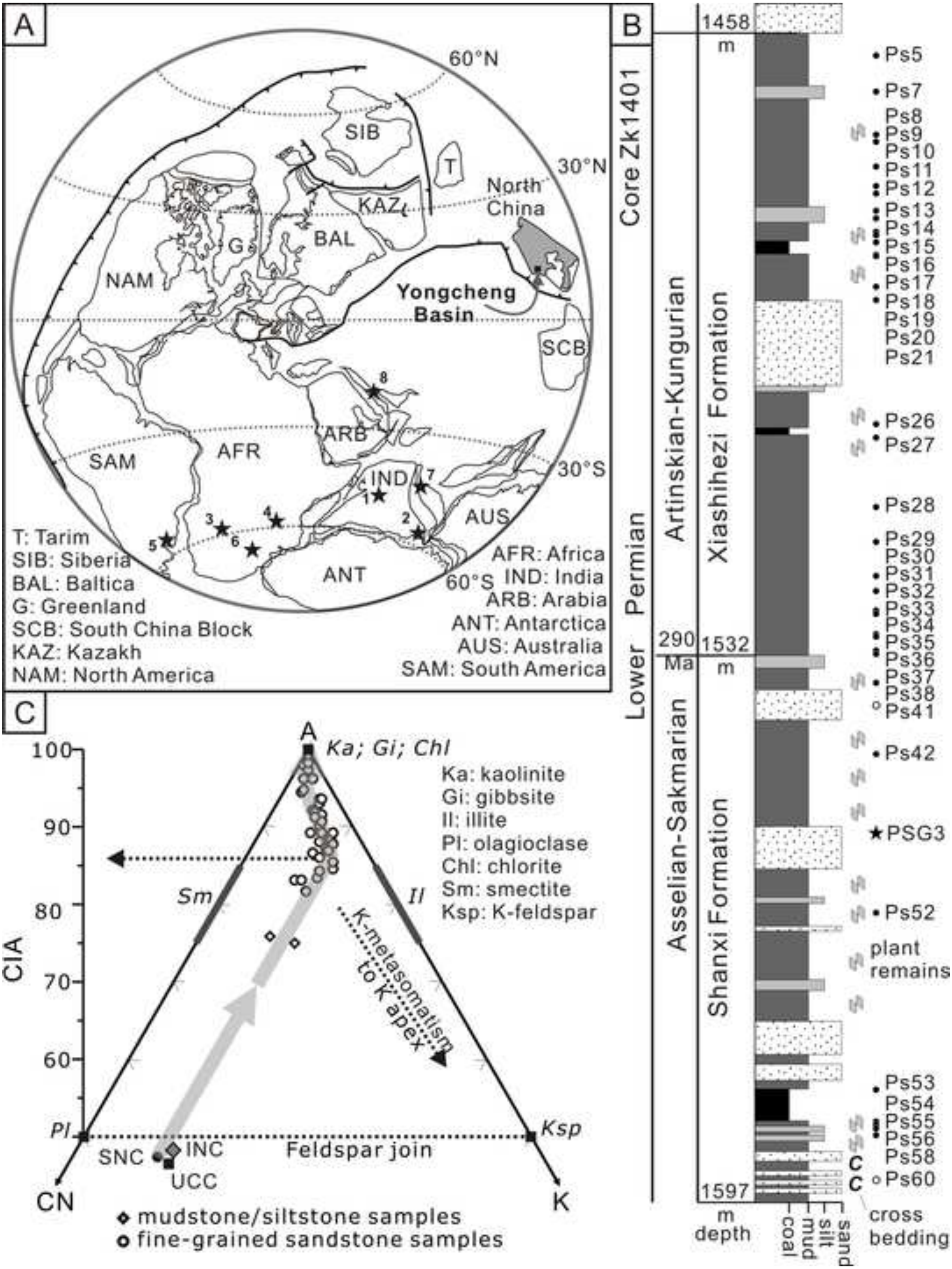

Figure 2

Click here to download high resolution image

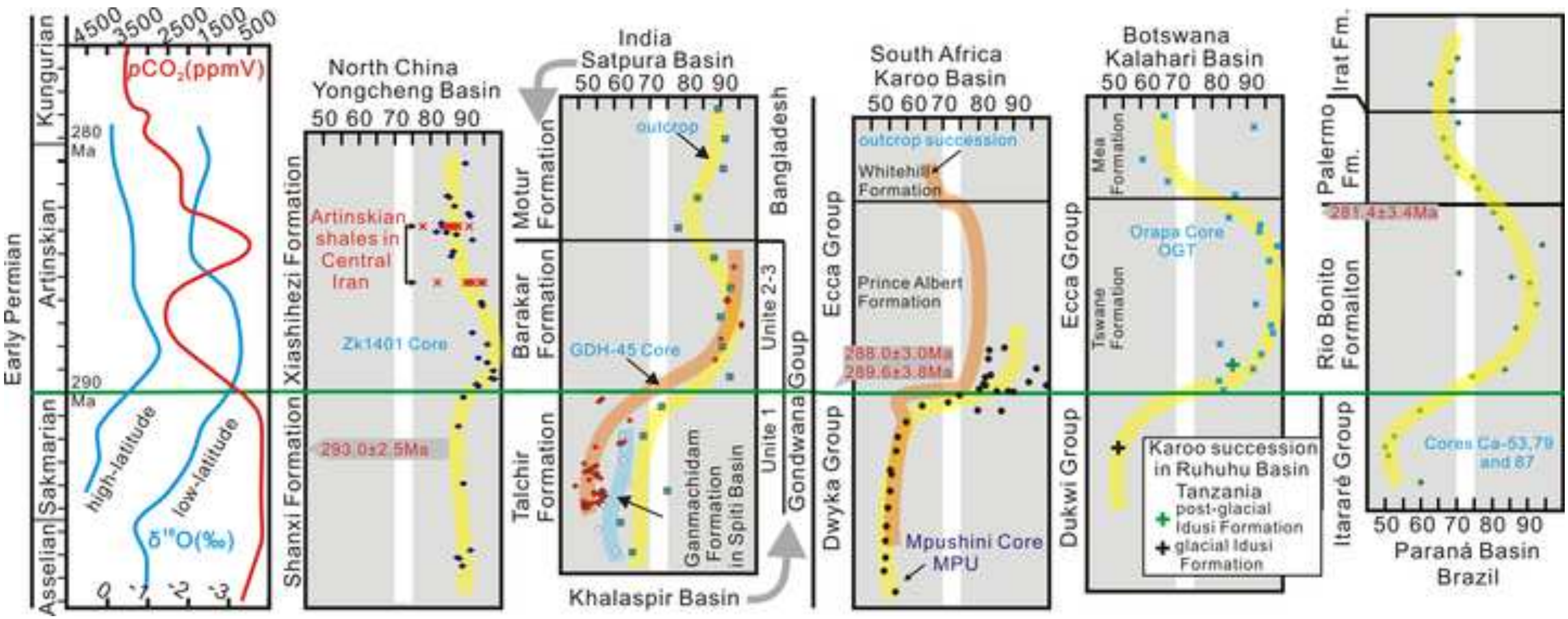

Figure 3

Click here to download high resolution image

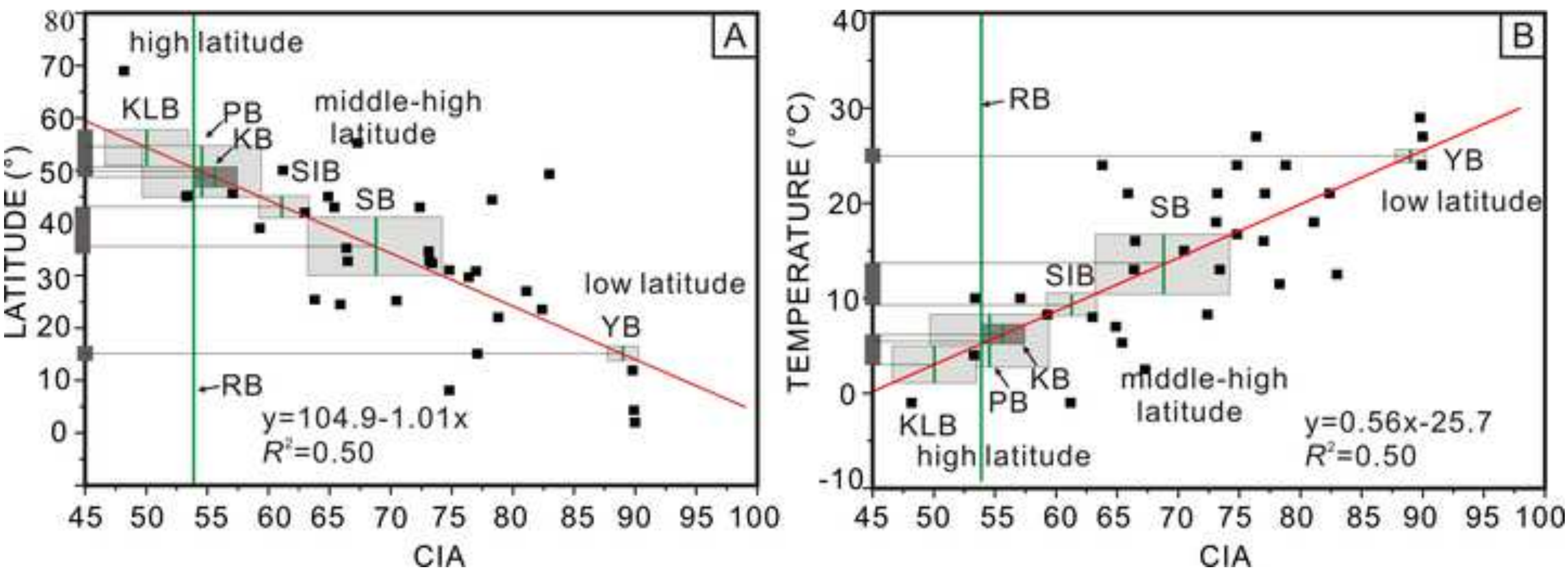

Supplemental file
Click here to download Supplemental file: G35892-Supplementary file.doc

GSA Data repository Item

Supplementary materials for:

Global continental weathering trends across the Early Permian glacial to postglacial transition: Correlating high and low paleo-latitude sedimentary records

Jianghai Yang[1*], Peter A. Cawood[2,3], Yuansheng Du[1], Bin Feng[4], Jiaxin Yan[1],
[1] State Key Laboratory of Biogeology and Environmental Geology, China University of Geosciences, Wuhan, 430074, China
[2] Department of Earth Sciences, University of St. Andrews, North Street, St. Andrews KY16 9AL, UK
[3] School of Earth and Environment, University of Western Australia, Crawley, WA 6009, Australia
[4] No.4 Institute of Geological & Mineral Resources Survey of Henan, Zhengzhou, 450016, China

ANALYTICAL PROCEDURES

Whole-rock major and trace element concentrations were determined with X-ray florescence and ICP-MS by ALS Chemex, and mineralogical X-Ray Diffraction analysis and zircon LA-ICPMS dating were conducted in the State Key Laboratory of Geological Process and Mineral Resources, China University of Geosciences (Wuhan).

1. U-Pb isotope LA-ICPMS analysis of zircons

Zircons were separated from sample PSG3 by conventional procedures before hand-picking under a binocular microscope, mounting in epoxy and polished. Back scatter electron (BSE) and cathodoluminescence (CL) images were conducted on a JEOL JXA-8100 electron microprobe. Representative CL images for the analyzed zircons are shown in Figure DR1. Prior to LA-ICPMS analysis, zircons were subject to washing with dilute HNO_3 in an ultrasonic bath to eliminate surface contamination. For the LA-ICPMS analyses, laser sampling was performed using a Geolas 2005, and ion-signal intensities were acquired by an Agilent 7500a ICP-MS instrument. The diameter of the laser spot was 32 μm. Each analysis incorporated a background acquisition of approximately 20-30 s (gas blank) followed by 50 s data acquisition from the sample. The Agilent Chemstation was utilized for the acquisition of each individual analysis. Detailed operating conditions for the laser ablation system and the ICP-MS instrument and data reduction are described by Liu et al. (2010). Zircon 91500 ($^{206}Pb/^{238}U$ age = 1062.4 ± 0.4 Ma, Wiedenbeck et al., 1995) was used as external standard for U-Pb dating, and was analyzed twice every 6 analyses. Off-line selection and integration of background and signals, and time-drift correction and quantitative calibration for trace element analyses and U-Pb dating were performed by ICPMSDataCal (Liu et al., 2010; Liu et al., 2008). Concordia diagrams and weighted mean calculations were made using Isoplt/Ex_ver3 (Ludwig, 2003). Zircon standards Gj-1 was analyzed as unknown and the obtained mean $^{206}Pb/^{238}U$ age is 599.1 ± 8.4 Ma (2σ) in line with the recommended age of 599.8 ± 1.7 Ma (2σ, Jackson et al., 2004).

2. Mineralogical X-Ray Diffraction analysis

X-ray diffraction (XRD) studies of samples were performed with a PANalytical X'Pert Pro using a Cu-Ni tube at 40 kV and 40 mA, under continuous scanning with a speed of 8°/min. The mass percentage (mass %) of the main mineral phases identified were semi-quantified with an analytical error of ± 10 %.

3. Whole-rock geochemical analysis

After removing surface layer, solid samples were grounded to less than 200 mesh. For elemental oxide concentration analysis, sample powders were mixed with dry lithium tetraborate and borate and fused to glass beads, and analytical performance was conducted on a PANalytical Axios X-ray florescence spectrometer with accuracy better than 5% and uncertainty less than 5 %. Trace element (Rb, Sr, Ba, and Zr) contents were obtained on Perkin Elmer Elan 9000 ICP-MS with accuracy better than 10 % and uncertainty less than 10 % for the analyzed elements after complete fusion of samples with lithium borate and dissolution in ultrapure HNO_3.

DATA REPOSITORTY FIGURE CAPTIONS

Figure DR1. A: Representative CL images for dated zircons; B: Tera-Wasserburg plot of zircon analyses from Sample PGS3, where the gray symbols mark the integrated analyses for calculating weighted average age [inset, 293.0 ± 2.5 Ma (n = 21, MSWD = 0.57)]. This average age is equal to the lower intercept age within error (290.0 ± 3.0 Ma) and interpreted as the depositional age of this tuffaceous bed. Another three concordant analyses gave Paleoproterozoic $^{207}Pb/^{206}Pb$ ages (1832-1721 Ma, Table DR1), and are considered xenocrystic in origin.

Figure DR2. Stratigraphic variations of CIA value (chemical index of alteration, Nesbitt and Young, 1982), clay mineral assemblage, and provenance chemical indicator Zr/Ti ratio for silt-mudstone samples. Other chemical weathering indices including weathering index of Parker (WIP, Parker, 1970), chemical index of weathering (CIW, Harnois, 1988), plagioclase index of alteration (PIA, Fedo et al., 1995) and CIA_{molar} (expressed as $Al_2O_3/(CaO^*+Na_2O+K_2O)$ mole ratio, Goldberg and Humayun, 2010) were also plotted for comparison. CaO* involved in index calculations represent only the Ca in silicate fractions.

REFERENCES CITED

Goldberg, K., and Humayun, M., 2010, The applicability the Chemical Index of Alteration as a paleoclimatic indicator: an example from the Permian of the Paraná Basin, Brazil: Palaeogeography, Palaeoclimatology, Palaeoecology, v. 293, p. 175-183.

Harnois, L., 1988, The CIW index: a new chemical index of weathering: Sedimentary Geology, v. 55, p. 319-322.

Jackson SE, Pearson NJ, Griffin WL, Belousova EA. 2004. The application of laser ablation-inductively coupled plasma-mass spectrometry to in situ U-Pb zircon geochronology. Chemical Geology, v. 211, p. 47-69.

Liu, Y., Gao, S., Hu, Z., Gao, C., and Zong, K., 2010, Continental and oceanic crust recycling-induced melt-peridotite interactions in the Trans-North China Orogen: U-Pb dating, Hf isotopes and trace elements in zircons of mantle xenoliths: Journal of Petrology, v. 51, p. 537-571.

Liu, Y., Zong, K., Kelemen, P.B., and Gao, S., 2008, Geochemistry and magmatic history of eclogites and ultramafic rocks from the Chinese continental scientific drill hole: subduction and ultrahigh-pressure metamorphism of lower crustal cumulates: Chemical Geology, v. 247, p. 133-153.

Nesbitt, H.W., and Young, G.M., 1982, Early Proterozoic climates and plate motions inferred from major element chemistry of lutites: Nature, v. 299, p. 715-717.

—, 1984, Prediction of some weathering trends of plutonic and volcanic rocks based on thermodynamic and kinetic considerations: Geochimica et Cosmochimica Acta, v. 48, p. 1523-1534.

Ludwig K.R. 2003. User`s manual for Isoplot 3.00: a geochronological toolkit for microsoft Excel: Berkeley

Parker, A., 1970, An index of weathering for silicate rocks: Geological Magazine, v. 107, p. 501-504.

Wiedenbeck, M., Allé, P., Corfu, F., Griffin, W.L., Meier, M., Oberli, F., von Quadt, A., Roddick, J.C, Spiegel, W., 1995. Three natural zircon standards for U-Th-Pb, Lu-Hf, trace element and REE analyses. Geostand. Newsl., v. 19, p.1-23.

Table DR1. Zircon U-Pb isotope data for tuffaceous sandstone Sample PSG3

Spot	Pb	Th	U	Th/U	207Pb/206Pb		207Pb/235U		206Pb/238U		rho	207Pb/206Pb		207Pb/235U		206Pb/238U		Concordance
	ppm	ppm	ppm		Ratio	±1σ	Ratio	±1σ	Ratio	±1σ		Age (Ma)	±1σ	Age (Ma)	±1σ	Age (Ma)	±1σ	
PSG3-1	45.0	119	132	0.90	0.0550	0.0045	0.3649	0.0262	0.0499	0.0010	0.2875	409	183	316	20	314	6	99%
PSG3-2	18.0	84.0	118	0.71	0.0572	0.0041	0.3602	0.0254	0.0459	0.0008	0.2529	498	159	312	19	289	5	92%
PSG3-3	27.9	134	152	0.88	0.0542	0.0047	0.3377	0.0283	0.0458	0.0010	0.2565	389	196	295	21	289	6	97%
PSG3-4	18.6	91.8	108	0.85	0.0540	0.0050	0.3337	0.0299	0.0459	0.0010	0.2347	372	209	292	23	289	6	98%
PSG3-5	21.1	108	118	0.92	0.0554	0.0037	0.3524	0.0242	0.0465	0.0011	0.3460	428	150	307	18	293	7	95%
PSG3-6	31.8	149	183	0.81	0.0476	0.0031	0.3177	0.0207	0.0487	0.0010	0.3071	80	148	280	16	306	6	91%
PSG3-7	23.4	107	132	0.81	0.0526	0.0040	0.3240	0.0239	0.0460	0.0010	0.3002	322	174	285	18	290	6	98%
PSG3-8	22.6	102	126	0.82	0.0520	0.0033	0.3276	0.0208	0.0465	0.0010	0.3440	283	153	288	16	293	6	98%
PSG3-9	18.7	77.3	121	0.64	0.0663	0.0051	0.4525	0.0374	0.0504	0.0015	0.3526	817	156	379	26	317	9	82%
PSG3-10	112	74.2	97.8	0.76	0.1122	0.0036	5.3605	0.1810	0.3461	0.0048	0.4117	1836	59	1879	29	1916	23	98%
PSG3-11	31.4	150	208	0.72	0.0535	0.0038	0.3402	0.0223	0.0476	0.0010	0.3246	346	163	297	17	300	6	99%
PSG3-12	15.6	69.9	111	0.63	0.0558	0.0044	0.3649	0.0277	0.0479	0.0011	0.3110	443	174	316	21	302	7	95%
PSG3-13	19.9	95.6	127	0.75	0.0539	0.0049	0.3422	0.0298	0.0475	0.0012	0.2870	369	206	299	23	299	7	99%
PSG3-14	19.4	80.0	134	0.60	0.0623	0.0046	0.3941	0.0284	0.0465	0.0010	0.2967	687	158	337	21	293	6	85%
PSG3-15	12.8	60.0	84.9	0.71	0.0637	0.0059	0.4135	0.0366	0.0475	0.0012	0.2839	731	196	351	26	299	7	83%
PSG3-16	18.4	83.4	90.6	0.92	0.0815	0.0068	0.5083	0.0423	0.0455	0.0012	0.3134	1235	165	417	28	287	7	63%
PSG3-17	20.1	85.1	154	0.55	0.0568	0.0044	0.3708	0.0269	0.0482	0.0010	0.3007	483	175	320	20	304	6	94%
PSG3-18	12.9	58.3	87.8	0.66	0.0522	0.0049	0.3385	0.0312	0.0482	0.0012	0.2647	300	217	296	24	303	7	97%
PSG3-19	12.8	51.8	80.6	0.64	0.0629	0.0053	0.4089	0.0344	0.0473	0.0011	0.2792	706	175	348	25	298	7	84%
PSG3-20	16.3	80.5	108	0.74	0.0563	0.0046	0.3724	0.0330	0.0478	0.0011	0.2689	465	183	321	24	301	7	93%
PSG3-21	18.6	88.0	125	0.71	0.0541	0.0042	0.3450	0.0263	0.0465	0.0011	0.3014	376	174	301	20	293	7	97%
PSG3-22	17.7	83.8	93.7	0.89	0.0704	0.0060	0.4387	0.0346	0.0478	0.0012	0.3220	939	176	369	24	301	7	79%
PSG3-23	21.6	92.4	143	0.65	0.0578	0.0048	0.3761	0.0306	0.0470	0.0009	0.2271	524	183	324	23	296	5	90%
PSG3-24	142	717	571	1.26	0.0568	0.0025	0.3671	0.0169	0.0463	0.0007	0.3408	483	103	318	13	292	4	91%
PSG3-25	15.0	66.0	90.8	0.73	0.0569	0.0055	0.3545	0.0305	0.0474	0.0012	0.2930	487	215	308	23	298	7	96%
PSG3-26	11.3	54.0	91.8	0.59	0.0679	0.0063	0.4446	0.0374	0.0486	0.0012	0.2985	878	194	373	26	306	8	80%
PSG3-27	15.2	75.6	110	0.69	0.0636	0.0053	0.3785	0.0288	0.0445	0.0010	0.2839	728	177	326	21	281	6	85%
PSG3-28	29.6	143	203	0.71	0.0543	0.0037	0.3351	0.0213	0.0456	0.0009	0.3201	383	149	293	16	288	6	98%
PSG3-29	16.6	77.4	114	0.68	0.0570	0.0050	0.3636	0.0295	0.0481	0.0011	0.2785	500	193	315	22	303	7	96%
PSG3-30	13.5	53.9	74.5	0.72	0.0638	0.0056	0.3996	0.0344	0.0464	0.0012	0.3001	744	185	341	25	293	7	84%
PSG3-31	15.3	75.2	117	0.64	0.0531	0.0036	0.3286	0.0213	0.0456	0.0010	0.3375	345	154	288	16	288	6	99%
PSG3-32	37.7	167	228	0.73	0.0557	0.0033	0.3577	0.0212	0.0471	0.0008	0.2980	439	135	310	16	296	5	95%
PSG3-33	12.5	52.9	75.6	0.70	0.0693	0.0058	0.4443	0.0378	0.0469	0.0014	0.3402	906	173	373	27	295	8	76%
PSG3-34	20.2	88.0	124	0.71	0.0593	0.0046	0.3635	0.0251	0.0462	0.0010	0.3091	589	136	315	19	291	6	92%

PSG3-35	11.5	54.7	74.3	0.74	0.0663	0.0068	0.3956	0.0388	0.0446	0.0011	0.2584	817	214	338	28	281	7	81%
PSG3-36	58.1	34.8	77.9	0.45	0.1063	0.0043	4.7052	0.1983	0.3210	0.0054	0.4027	1737	74	1768	35	1794	27	98%
PSG3-37	28.9	136	136	1.00	0.0553	0.0044	0.3620	0.0273	0.0484	0.0011	0.3142	433	181	314	20	305	7	97%
PSG3-38	19.6	31.5	43.0	0.73	0.2131	0.0192	1.6076	0.1256	0.0582	0.0022	0.4861	2929	146	973	49	365	13	9%
PSG3-39	33.9	161	165	0.97	0.0600	0.0042	0.3724	0.0255	0.0458	0.0010	0.3051	611	154	321	19	288	6	89%
PSG3-40	18.6	88.8	115	0.78	0.0537	0.0045	0.3446	0.0268	0.0469	0.0008	0.2294	361	189	301	20	295	5	98%
PSG3-41	41.7	205	223	0.92	0.0579	0.0034	0.3616	0.0206	0.0453	0.0008	0.3154	528	130	313	15	286	5	90%
PSG3-42	14.7	72.1	96.8	0.74	0.0592	0.0053	0.3676	0.0324	0.0460	0.0012	0.2842	576	199	318	24	290	7	90%
PSG3-43	25.3	130	107	1.21	0.0631	0.0049	0.3949	0.0285	0.0455	0.0010	0.2987	722	169	338	21	287	6	83%
PSG3-44	14.4	69.4	99.3	0.70	0.0568	0.0053	0.3570	0.0348	0.0458	0.0012	0.2782	483	209	310	26	289	8	92%
PSG3-45	60.0	300	381	0.79	0.0538	0.0025	0.3455	0.0163	0.0462	0.0007	0.3171	365	112	301	12	291	4	96%
PSG3-46	11.1	50.0	84.0	0.60	0.0591	0.0048	0.3700	0.0299	0.0461	0.0011	0.3075	572	178	320	22	290	7	90%
PSG3-47	60.4	45.4	33.3	1.36	0.1050	0.0045	4.8545	0.2011	0.3347	0.0055	0.3984	1714	78	1794	35	1861	27	96%
PSG3-48	23.1	108	157	0.69	0.0514	0.0042	0.3426	0.0272	0.0486	0.0010	0.2521	261	185	299	21	306	6	97%
PSG3-49	18.5	91.0	116	0.79	0.0541	0.0049	0.3450	0.0290	0.0476	0.0010	0.2604	376	201	301	22	299	6	99%
PSG3-50	15.0	72.6	85.7	0.85	0.0686	0.0051	0.4166	0.0274	0.0458	0.0011	0.3583	887	154	354	20	289	7	79%
PSG3-51	25.9	132	116	1.15	0.0548	0.0045	0.3363	0.0279	0.0456	0.0010	0.2691	406	190	294	21	287	6	97%
PSG3-52	14.5	63.5	85.3	0.74	0.0576	0.0053	0.4062	0.0367	0.0514	0.0012	0.2646	522	203	346	26	323	8	93%
PSG3-53	43.5	228	221	1.03	0.0553	0.0038	0.3586	0.0248	0.0474	0.0010	0.2958	433	156	311	19	299	6	95%
PSG3-54	13.2	62.3	87.9	0.71	0.0564	0.0049	0.3554	0.0311	0.0460	0.0010	0.2516	478	193	309	23	290	6	93%
PSG3-55	124	659	404	1.63	0.0507	0.0025	0.3256	0.0157	0.0470	0.0008	0.3516	233	118	286	12	296	5	96%
PSG3-56	5.70	28.6	42.5	0.67	0.0769	0.0083	0.4345	0.0458	0.0460	0.0016	0.3291	1120	217	366	32	290	10	76%
PSG3-57	22.8	107	135	0.79	0.0549	0.0043	0.3381	0.0265	0.0454	0.0010	0.2706	409	169	296	20	286	6	96%
PSG3-58	16.1	74.8	106	0.70	0.0535	0.0050	0.3261	0.0280	0.0458	0.0011	0.2683	350	209	287	21	289	7	99%
PSG3-59	17.6	79.3	118	0.67	0.0574	0.0044	0.3652	0.0254	0.0477	0.0009	0.2776	509	201	316	19	300	6	94%
PSG3-60	21.8	92.1	128	0.72	0.0557	0.0044	0.3517	0.0257	0.0475	0.0012	0.3385	443	178	306	19	299	7	97%

Table DR2. XRD mineralogical composition of the Lower Permian samples from southeastern North China

Samples	Depth (m)	Quartz	Feldspar	Calcite	Siderite	Clay minerals	Clay mineral assemblage		
							Chlorite	Illite	Kaolinite
ps5	1460	34	0	0	2	64	35	25	40
ps7	1465	27	0	0	46	27	5	20	75
ps8	1470.5	33	0	0	6	61	15	35	50
ps9	1471.1	38	0	0	2	60	15	25	60
ps10	1473.9	38	2	0	3	57	20	20	60
ps11	1476.3	32	0	0	2	66	15	15	70
ps12	1477.2	30	2	0	2	66	15	20	65
ps13	1479.4	40	6	2	2	50	20	25	55
ps14	1480.5	33	3	0	3	61	25	25	50
ps15	1482.2	33	3	0	3	61	25	25	50
ps16	1482.4	34	3	0	2	61	20	20	60
ps17	1483.1	32	2	0	2	64	15	15	70
ps19	1484.7	34	0	0	0	66	15	15	70
ps20	1488.5	29	0	0	16	55	10	10	80
ps21	1490	32	2	0	4	62	20	20	60
ps26	1505	10	0	2	0	88	10	10	80
ps27	1506	14	0	0	0	86	15	10	75
ps28	1514.7	38	0	0	2	60	15	10	75
ps29	1518.6	32	2	0	0	66	15	5	80
ps30	1522.8	32	0	0	2	66	15	10	75
ps31	1524.5	4	0	0	0	96	10	10	80
ps33	1527	2	0	0	32	66	30	0	70
ps34	1529.5	46	0	0	5	49	20	5	75
ps35	1529.6	4	0	0	0	96	35	10	55
ps36	1531.5	24	0	0	0	76	65	20	15
ps37	1532	29	0	0	2	69	55	15	30
ps38	1535.6	29	2	0	0	69	25	25	50
ps42	1545	39	3	0	2	56	25	25	50
ps52	1564.8	34	2	0	0	64	25	25	50
ps53	1585	35	0	0	0	65	20	25	55
ps54	1587.7	40	2	0	2	56	15	25	60
ps55	1587.8	43	2	0	2	53	15	30	55
ps58	1590	35	2	0	2	61	10	20	70

Table DR3. Whole-rock major element (%) and trace element (ppm) geochemistry of the Lower Permian samples from southeastern North China

Sample	Depth (m)	Lithology	SiO_2	Al_2O_3	Fe_2O_3	CaO	MgO	Na_2O	K_2O	TiO_2	MnO	P_2O_5	LOI	Total	Rb	Sr	Ba	Zr
ps5	1460	mudstone	57.02	24.15	5.1	0.16	0.67	0.45	1.61	0.91	0.01	0.04	9.77	99.94	91.8	122.5	464	196
ps7	1465	siltstone	28.97	8.13	37.47	1.04	1.21	0.29	0.63	0.38	0.43	0.171	21.3	100.05	36.8	66.2	216	163
ps8	1470.5	mudstone	54.39	20.58	8.68	0.22	0.76	0.53	2.39	0.83	0.3	0.062	10.6	99.42	150.5	119.5	630	185
ps9	1471.1	mudstone	61.38	21.06	4.71	0.14	0.76	0.55	2.32	0.97	0.13	0.041	7.89	100	139	109.5	581	216
ps10	1473.9	mudstone	59.23	21.15	5.63	0.28	0.85	0.53	2.01	0.98	0.07	0.139	8.92	99.85	119.5	121	500	246
ps11	1476.3	mudstone	55.47	26.15	3.36	0.14	0.56	0.49	1.65	0.85	0.01	0.063	10.75	99.56	91.8	149	512	169
ps12	1477.2	mudstone	54.45	27.14	3.16	0.15	0.52	0.52	1.46	0.79	0.01	0.054	11.65	99.95	82.9	138	503	165
ps13	1479.4	siltstone	63.8	20.58	2.77	0.35	0.73	1.07	1.77	0.94	0.01	0.074	7.37	99.53	91.7	145	471	367
ps14	1480.5	siltstone	58.79	21.45	5.02	0.35	1.06	0.84	2.23	0.88	0.09	0.083	9.07	99.95	113.5	149.5	566	196
ps15	1482.2	mudstone	59	19.83	6.07	0.57	1.06	0.89	2	0.84	0.11	0.099	9.13	99.66	99.6	138.5	489	215
ps16	1482.4	mudstone	58.3	22.2	4.03	0.31	0.93	0.8	2.23	0.91	0.05	0.083	9.23	99.14	115	157.5	573	216
ps17	1483.1	mudstone	60.29	23.96	2.32	0.17	0.61	0.58	2.16	0.99	0.01	0.043	8.76	99.95	94.2	147	510	225
ps19	1484.7	mudstone	56.19	27	2	0.14	0.4	0.51	1.22	0.79	0.01	0.028	11.35	99.69	50.4	149.5	419	184
ps20	1488.5	mudstone	46.74	18.9	14.79	0.38	0.86	0.57	1.49	0.82	0.19	0.139	14.55	99.49	68.6	169.5	421	293
ps21	1490	mudstone	58.46	20.56	5.71	0.28	0.85	0.68	1.84	0.87	0.08	0.122	10.4	99.91	84.8	169.5	457	243
ps26	1505	mudstone	38.09	26.81	2.48	0.2	0.43	0.41	0.54	0.53	0.01	0.029	29.6	99.17	23.1	140.5	327	231
ps27	1506	mudstone	41.13	28.87	2.05	0.15	0.42	0.46	0.63	0.58	0.01	0.027	24.6	98.97	26.4	156.5	373	253
ps28	1514.7	mudstone	62.11	22.58	3.29	0.1	0.45	0.45	1.12	1.05	0.01	0.053	8.57	99.84	58.6	130.5	375	374
ps29	1518.6	mudstone	53.75	30.38	1.65	0.12	0.22	0.38	0.42	0.99	0.01	0.032	12.1	100.1	19.3	140	263	313
ps30	1522.8	mudstone	58.21	25.44	3	0.08	0.37	0.3	1.17	1.03	0.03	0.054	9.8	99.56	63.6	162	319	277
ps31	1524.5	mudstone	44.5	37.33	1.33	0.08	0.24	0.31	0.95	0.99	0.01	0.061	13.85	99.69	40.6	186	385	335
ps33	1527	mudstone	32.22	27.56	19.32	0.13	0.34	0.16	0.18	1.01	0.16	0.033	18.25	99.39	8.2	78.4	103	411
ps34	1529.5	mudstone	67.09	18.4	4.48	0.03	0.19	0.13	0.27	0.65	0.02	0.033	7.88	99.18	11.5	74	103.5	310
ps35	1529.6	mudstone	42.34	35.51	5.65	0.26	0.22	0.22	0.33	1.35	0.01	0.243	13.5	99.67	15.2	205	273	583
ps36	1531.5	mudstone	48.17	23.79	16.36	0.18	0.81	0.33	1.15	0.86	0.01	0.196	7.72	99.65	53.6	351	374	231
ps37	1532	mudstone	51.02	23.73	12.35	0.14	0.68	0.25	1.11	0.84	0.02	0.12	9.09	99.41	53.1	230	312	252
ps38	1535.6	mudstone	56.98	25.51	3.04	0.19	0.63	0.76	1.52	0.98	0.01	0.081	9.71	99.49	60	253	713	412
ps41	1538	fine–grained	63.02	20.29	3.25	0.91	0.7	1.8	1.96	0.75	0.01	0.132	6.96	99.89	65.9	265	704	207
ps42	1545	mudstone	60.76	23.51	1.98	0.08	0.49	0.75	1.8	0.9	0.01	0.048	8.98	99.39	83.9	171.5	551	296
ps52	1564.8	mudstone	53.63	26.74	1.48	0.07	0.49	0.69	1.94	0.74	0.01	0.056	13.85	99.74	89.5	130.5	431	210
ps53	1585	mudstone	46.65	23.11	1.32	0.07	0.39	0.43	1.37	0.72	0.01	0.071	25.5	99.68	65.9	142.5	285	224
ps54	1587.7	mudstone	62.46	23.16	1.17	0.1	0.36	0.44	2.06	0.91	0.01	0.027	8.96	99.71	79.3	121	526	482
ps55	1587.8	mudstone	62.32	22.4	1.29	0.12	0.37	0.4	2.14	1.02	0.01	0.031	9.13	99.29	83.3	119.5	520	579
ps58	1590	mudstone	60.55	22.12	1.31	0.05	0.4	0.4	1.88	0.69	0.01	0.038	12.35	99.85	68.5	94.9	432	279
ps60	1594.5	fine–grained	50.49	15.18	12.91	1.09	1.79	0.84	2.09	0.65	0.29	0.132	13.8	99.35	81.8	199	492	274

Figure DR1

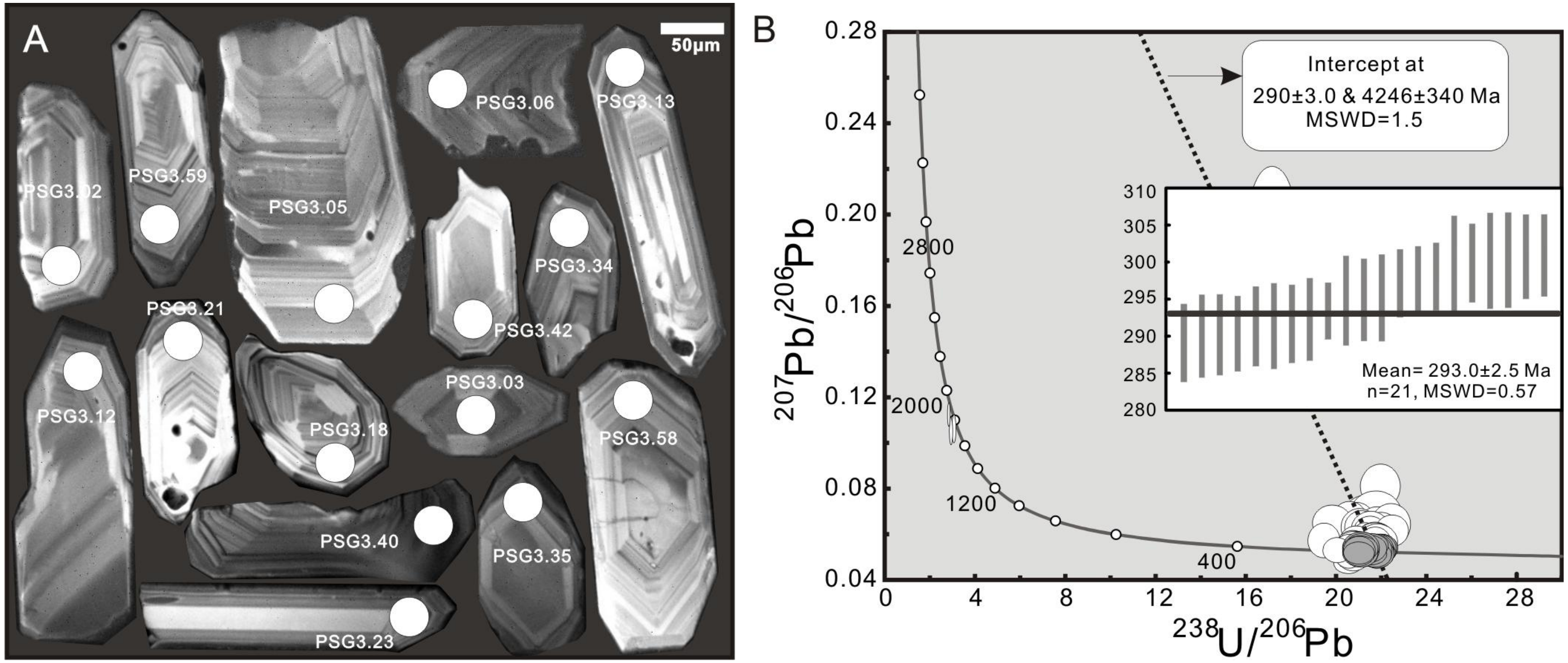

A
50μm
PSG3.02
PSG3.59
PSG3.05
PSG3.06
PSG3.13
PSG3.34
PSG3.21
PSG3.42
PSG3.12
PSG3.03
PSG3.18
PSG3.58
PSG3.40
PSG3.35
PSG3.23
B
Intercept at
290±3.0 & 4246±340 Ma
MSWD=1.5
Mean= 293.0±2.5 Ma
n=21, MSWD=0.57
2800
2000
1200
400
$^{207}Pb/^{206}Pb$
$^{238}U/^{206}Pb$

Figure DR2

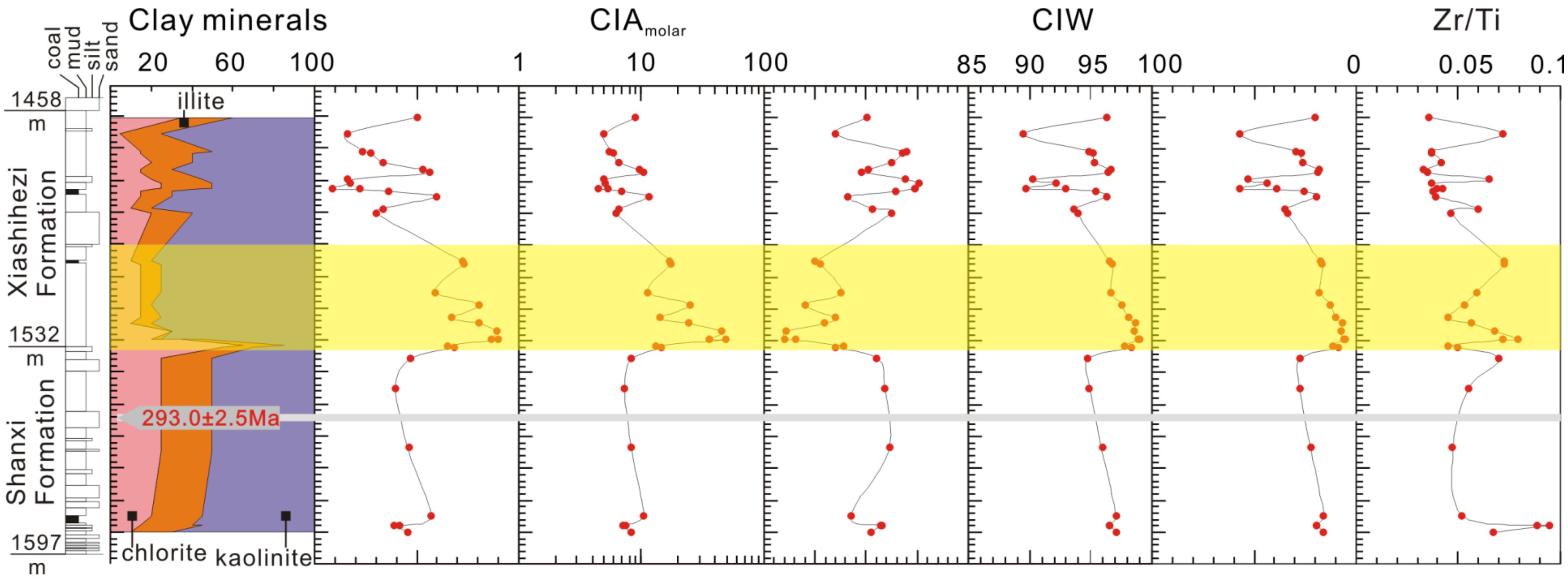

coal
mud
silt
sand
Clay minerals
20
60
100
CIA
molar
1
10
100
CIW
85
90
95
100
Zr/Ti
0
0.05
0.1
1458
m
illite
Xiashihezi
Formation
1532
m
Shanxi
Formation
293.0±2.5Ma
1597
m
chlorite
kaolinite
80
90
100
CIA
0
10
20
30
40
WIP
80
90
100
PIA